Optics Letters

Dynamic curvature sensing using time expanded ΦOTDR

Camilo Escobar-Vera,[1,*] Miguel Soriano-Amat,[1] Hugo F. Martins,[2] David Barrera,[3] Sonia Martin-Lopez,[1] Miguel Gonzalez-Herraez,[1] and María R. Fernández-Ruiz[1]

[1]Universidad de Alcalá, Photonics Engineering Group, 28805 Madrid, Spain
[2]Instituto de Óptica "Daza de Valdés", IO-CSIC, C/Serrano 121, 28006 Madrid, Spain
[3]PRL, Photonics Research Labs, Universitat Politècnica de València, Camino de Vera s/n, 46022 Valencia, Spain
*camilo.escobar@uah.es

Received 15 May 2023; revised 6 July 2023; accepted 13 July 2023; posted 13 July 2023; published 00 xxxxxx 0000

Shape sensing can be accomplished using optical fiber sensors through different interrogation principles such as fiber Bragg gratings, optical frequency-domain reflectometry (OFDR), or optical time-domain reflectometry (OTDR). These techniques are either not entirely distributed, have poor performance in dynamic sensing, or are only valid for few-meter-long fibers. Here, we present a system able to perform distributed curvature sensing with a range of 125 m, 10-cm resolution, and a sampling rate of 50 Hz. This is done by interrogating three cores of a multi-core fiber (MCF) with the novel time-expanded phase-sensitive (TE-Φ)OTDR technique. This system fills a performance gap in fiber shape sensors, opening the door to applications in civil engineering, medicine, or seismology.

https://doi.org/10.1364/OL.494466

The development of optical fiber sensors (OFSs) has made them an attractive option in an increasing number of fields due to the advantages they offer (e.g., flexibility, lightweight, robustness against hazardous conditions, possibility of remote sensing, etc.). In particular, distributed optical fiber sensors (DOFSs) are able to measure strain and temperature at any position along the fiber. These features can be used for shape sensing by performing directional strain measurements in multi-core fibers (MCFs).

In the literature, different approaches have been proposed to perform shape sensing. Fiber Bragg grating (FBG) techniques are widely used in this application [1]. This kind of sensor is able to reach a spatial resolution of centimeters. The MCFs used can either have straight cores (i.e., parallel to the fiber longitudinal axis) or helical, showing better performance in twist measurements [2,3]. Since one FBG is required for each position, these sensors are not fully distributed, are not able to reach very long ranges, and require an additional manufacturing process that significantly increases costs. However, distributed shape sensors are based on backscattering mechanisms, namely Brillouin and Rayleigh. Brillouin-based distributed shape sensors can perform absolute strain measurements along the fiber [4] and can reach up to 1-km ranges by interrogating MCFs [5]. Since the scattering process is very weak, measurements rely on large averaging processes that slow down the performance, limiting these schemes to static or almost static measurements. Rayleigh based shape sensors use optical frequency-domain reflectometry (OFDR) or optical time-domain reflectometry (OTDR) approaches to interrogate the backscattered light of the fiber. OFDR systems stand out for their capacity to reach short spatial resolutions (as short as millimeters) and high strain sensing accuracy [6], but with notably less range than OTDR. Among the different OTDR methods, phase-sensitive OTDR (ΦOTDR) is generally considered as the best solution to detect and quantify dynamic perturbations [7]. In ΦOTDR, changes in the phase of the backscattered light are detected and converted into local strain. ΦOTDR can reach up to km ranges with kHz sampling rates with the disadvantage of only attaining resolutions of the order of meters.

Recently, a new ΦOTDR approach has been proposed. This technique is called time-expanded (TE-)ΦOTDR and it is based on the use of a dual frequency comb (DFC). In this interrogation method, a probe comb is sent into the fiber and the backscattered light is beaten with a local oscillator (LO) comb. The two involved combs have a slight mismatch in the line spacing that induces a multi-heterodyne process that downconverts the optical traces to the radio frequency (RF) domain. This way, spatial resolutions of centimeters (i.e., bandwidths of GHz) can be detected with MHz photodetectors. This frequency downconversion imposes a reduction in sampling rates. However, cm resolutions can be readily obtained with sampling rates of 10–100 Hz, making this technique an appealing solution to perform real-time shape sensing in medium size structures [8].

In this paper, we show a system based on TE-ΦOTDR able to perform dynamic curvature sensing. First, we describe the methods used, specifically, we explain the mathematical link between strain and curvature, the experimental setup, and how the curvature is induced in the fiber. Then, the results are demonstrated, showing the performance of the system in curvature sensing. Lastly, some conclusions are provided.

To analyze the effect of curvature in an MCF, the cross section of a curved MCF is analyzed (Fig. 1). The curvature vector $\boldsymbol{\nu} = (\nu_1, \nu_2)$ marks the curvature of the fiber $\kappa = ||\boldsymbol{\nu}||$. The perpendicular direction of $\boldsymbol{\nu}$ defines the neutral axis, in which curvature

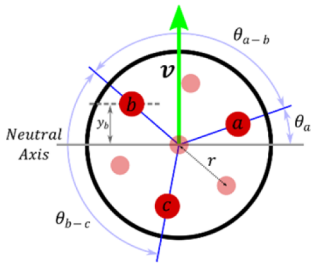

Fig. 1. Scheme of the cross section of the fiber. The seven cores are shown. Only the interrogated cores are shown in solid red. The neutral axis is shown in gray.

produces no strain change. This way, the points above the neutral axis will compress and those below will stretch.

Mathematically, the strain caused by curvature in each point ε_i depends on the distance to the neutral axis y_i according to the expression $\varepsilon_i = -\kappa \cdot y_i$. Since the three cores have the same distance r to the center core of the fiber, it is better to describe the position of the other three cores in terms of their angle θ_i or the angle difference θ_{a-i} with a reference angle (in this case, θ_a). Moreover, the strain estimation can also be affected by temperature fluctuations (given the cross-sensitivity of the phase to thermal and mechanical events) or common strain variation in the three cores. This contribution can be assumed common in each core due to their spatial proximity and is represented by the variable ε_T. The complete expression of the strain in each core is the following:

$$\begin{aligned}\varepsilon_i(z) &= -\kappa(z) \cdot r \cdot \cos(\theta_i) + \varepsilon_T(z) \\ &= -\kappa(z) \cdot r \cdot \cos(\theta_a + \theta_{a-i}) + \varepsilon_T(z)\end{aligned}, \tag{1}$$

The fiber used in the study has seven cores, the central core and six external cores forming the shape of a regular hexagon. As shown in Fig. 1, only three cores in a regular triangle disposition are interrogated. Because of this, the last expression can be particularized for the three cores a, b, and c with $\theta_{a-a} = 0$, $\theta_{a-b} = 2\pi/3$, and $\theta_{a-c} = 4\pi/3$ and expressed in matrix form,

$$\underbrace{\begin{pmatrix}\varepsilon_a(z)\\ \varepsilon_b(z)\\ \varepsilon_c(z)\end{pmatrix}}_{\boldsymbol{\varepsilon}(z)} = \underbrace{\begin{pmatrix}-r & 0 & 1\\ \frac{1}{2}r & \frac{\sqrt{3}}{2}r & 1\\ \frac{1}{2}r & -\frac{\sqrt{3}}{2}r & 1\end{pmatrix}}_{A} \underbrace{\begin{pmatrix}\kappa(z)\cos(\theta_a(z))\\ \kappa(z)\sin(\theta_a(z))\\ \varepsilon_T(z)\end{pmatrix}}_{\boldsymbol{\nu}_{\boldsymbol{\varepsilon}}(z)}, \tag{2}$$

where $\boldsymbol{\varepsilon}(z)$ is the strain vector containing the strain in each core, $\boldsymbol{A}$ is the coefficient matrix, and $\boldsymbol{\nu}_{\boldsymbol{\varepsilon}}(z)$ contains the curvature vector $\boldsymbol{\nu}(z)$ and the temperature contribution $\varepsilon_T(z)$. This equation can be solved for $\boldsymbol{\nu}(z)$, obtaining that $\boldsymbol{\nu}_{\boldsymbol{\varepsilon}}(z) = \boldsymbol{A}^+ \cdot \boldsymbol{\varepsilon}(z)$, where $\boldsymbol{A}^+$ is the inverse of $\boldsymbol{A}$. This way, curvature can be retrieved as $\kappa(z) = \sqrt{{\nu_1}^2(z) + {\nu_2(z)}^2}$, regardless of the fiber torsion [1].

To retrieve the strain in each core, an experimental setup is proposed. This experimental setup is based on a typical TE ΦOTDR architecture but slightly modified to obtain the strain of the three cores simultaneously. A scheme of the setup is shown in Fig. 2 (simplified from the actual one, for clarity). As can be observed, the light coming from the laser source is divided in a 90:10 coupler to generate the probe and LO signals (respectively). The two combs are generated with two Mach–Zehnder modulators (MZMs) that are fed with RF signals generated with an arbitrary

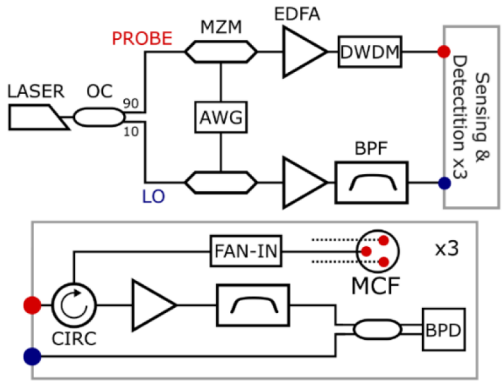

Fig. 2. Simplified scheme of the experimental setup. OC, optical coupler; MZM, Mach–Zehnder modulator; AWG, arbitrary waveform generator; EDFA, erbium-doped fiber amplifier; DWDM, dense wavelength division multiplexing; BPF, bandpass filter; BPD, balanced photodiode; CIRC, circulator.

waveform generator (AWG). Such RF signals are double sideband *ad hoc* designed signals with a comb-like spectrum similar to those implemented in previous reports of TE-ΦOTDR (e.g., in [9]). The combs have the same spectral phase so that the deconvolution process is automatic [9]. The probe comb is divided into three branches with approximately equal power and sent to the sensing and detection stage (Fig. 2). The LO comb is filtered, so that only one sideband is beaten with the backscattered signals from the cores, and also divided into three branches. The power split performed in both signals is carried out by means of optical couplers not shown in Fig. 2. In the sensing and detection stage, the probe comb is sent to the fan-in that guides the light to each of the interrogated cores. The backscattered light is amplified and filtered (to both reduce amplified spontaneous emission and retain a single sideband). Then, the outcome is beaten with the LO. This process is done for the three interrogated cores. The power split into three branches simply imposes a loss of signal-to-noise ratio in the traces as compared with a single-core scenario. Still, the spectral phase coding strategy ensures enough power to successfully obtain the strain. The three beat signals are photodetected with balanced photodiodes. In this proof of concept, the signals are acquired by an oscilloscope and processed offline.

In particular, we have performed a continuous acquisition that is digitally segmented and low-pass filtered to only include the first Nyquist zone [8]. This way, we obtain the optical trace in each instant for the three cores (with a sampling rate equal to the line spacing offset between the two combs). The traces include the backscattered light from the circulators, the single-core fibers (SCFs) in the fan-in, and the core of the MCF. Since the circulator and SCF section lengths are different for each channel, the traces have to be aligned numerically so that the information of the strain in the three cores in every position is correct. Then, the phase of the traces is demodulated and compared trace-to-trace.

To interpret the information correctly, an interpolation method based on the nearest neighbor analysis is applied to estimate the phase information associated with fading points [9].

The phase variation is then transformed into strain with the following expression:

$$\Delta\varepsilon = -\frac{\lambda_0}{S \cdot 2\pi \cdot 2n_0 \cdot \Delta z}\Delta\phi, \tag{3}$$

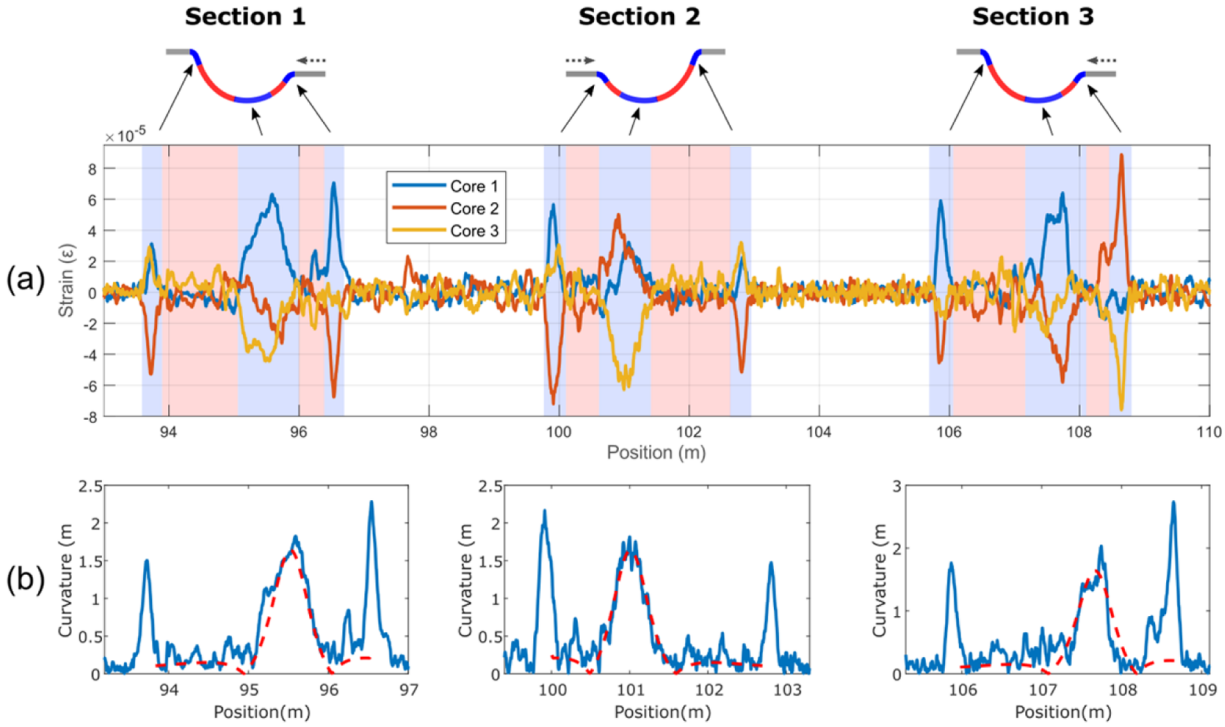

Fig. 3. (a) Strain profiles for the three cores of the MCF. An illustrative scheme of the catenary shape is shown for visual aid. The areas highlighted in red and blue are respectively those with lower and higher expected curvature change. (b) Distributed curvature. Curvature profiles in blue for the three sections and expected absolute curvature change in dotted red line obtained from simulated catenary.

where λ_0 is the wavelength of the laser, S is the strain factor (typically 0.78 [10]), n_0 is the refractive index of the fiber, and Δz is the gauge length. The gauge length is chosen so that the effect of the fading points is minimized in the distributed strain calculations. With the strain in each core, Eq. (2) can be solved and the values of curvature can be obtained.

To induce a controlled curvature in the MCF, three sections of a fiber are left hanging forming a catenary-like shape. The sections are consecutive and spaced so that the fiber between curved sections stays unperturbed. One end of the sections is fixed and the other end is movable. This end is manually moved horizontally so that the distance between the two extremes decreases and, consequently, the curvature varies along the fiber. This way we have three different sections of the fiber, corresponding to three catenaries that can be characterized simultaneously.

The measurements were made in a 112-m-long MCF. The sections left hanging were positioned near the end. The measurements were 40 s in duration with a sampling rate of 50 Hz. The three sections had lengths of $L = 2.85\ m$, $L = 2.93\ m$, and $L = 2.82\ m$, respectively. The height difference of the two ends is 75 cm for the three sections. The initial horizontal distance was $\Delta S_i = 2.12\ m$ and the final was $\Delta S_f = 1.45\ m$. This means that the initial curvature is non-zero and the results show strain variation and curvature variation. The probe and LO signals used correspond to a dual frequency comb with optical bandwidth of 5 GHz, line spacing of 800 kHz, and offset of 50 Hz which, in terms of sensing parameters, translates to a 2-cm spatial resolution, a maximum measurable fiber range of 125 m, and a sensing sampling rate of 50 Hz.

Figure 3(a) shows the strain for each core of the MCF. The values are shown after removing the mean of the three values of strain in each core that, as previously mentioned in the mathematical analysis, are not caused by curvature. The sections in which the fiber is hanging in a catenary-like shape are highlighted. The other sections correspond to the intermediate sections of fiber that are not perturbed. The three sections exhibit a similar pattern. Both ends of the sections show high values of strain variation in short lengths. This is due to the sudden curvature change between the fixed horizontal fiber section to the catenary-like shape section. Since the ends of the sections are fixed in different heights, the catenary shape is asymmetrical. The three sections are set so that the end of a section is the beginning of the next one. This way, sections 1 and 3 go from greater to lower height, and the opposite for section 2. Also, the maximum strain variation points are positioned next to the lower point (in the case of sections 1 and 3, to the right of the section center and in the case of section 2, to the left). This can be visualized in the illustrative scheme above in which the points with higher expected curvature, and consequently more strain difference in the cores, are shown in blue and those with lower curvature are shown in red. Note the difference between the horizontal distance axis and the optical distance or fiber arc length. The shape of the catenary is expressed in terms of the physical distance and the strain values are expressed in terms of the fiber length.

The curvature profiles obtained from the differential strain measurements can be seen in Fig. 3(b) for each section in blue. Near the ends, a high and narrow curvature peak can be observed in the three sections. The highest value corresponds to the end positioned at a lower height. A wider peak in curvature is observed near the low end of the catenary.

These values agree qualitatively with the expected asymmetrical shape shown in the illustrative scheme shown above in Fig. 3. The expected curvature profiles obtained from simulating

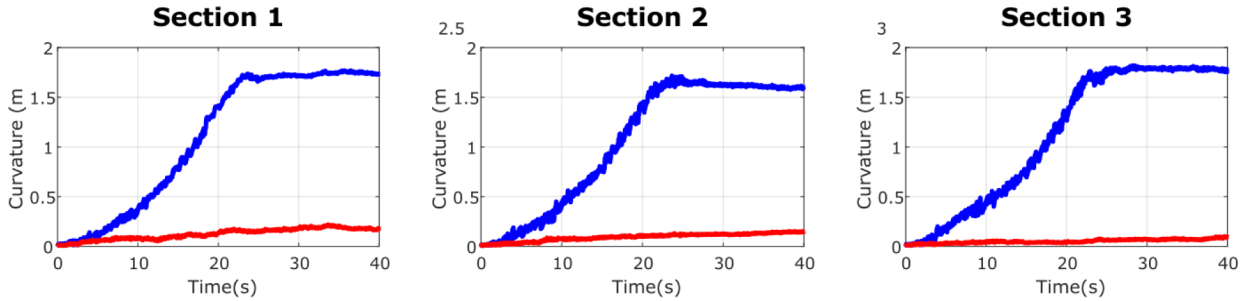

Fig. 4. Dynamic curvature for the three sections. Curvature of the highest curvature point as a function of time in blue and curvature of an unperturbed point as a function of time in red.

a catenary shape with the parameters of our setup are shown by the dotted red line. The simulated curvature variation profiles agree with the expected values in the central part of the sections.

To characterize the dynamic performance of the system, the curvature variations as a function of time are shown in Fig. 4. The values are shown for two points in the fiber: the point with the highest curvature within the catenary, in blue, and a non-perturbed point, in red. In the three cases, the blue line shows a progressive increase in curvature until $t = 23s$ (when the stimulus ends) and a flat temporal profile afterward. Additionally, the red line shows a slow increase with time, probably caused by error accumulation due to phase noise. This is an unavoidable drawback of ΦOTDR architectures. However, the maximum curvature values for these points are, in the worst-case scenario, approximately $0.2m^{-1}$ in the 40-seconds measurements, making this technique a valid solution to monitor curvature of the order of $1m^{-1}$ over periods of time of the order of 1 minute.

This way, we have shown a system able to perform dynamic curvature sensing with a TE-ΦOTDR-based architecture. This performance test proves that, by interrogating three cores in an MCF, we can detect curvatures in ranges up to 125 m, with a gauge length of 10 cm and a sampling rate of 50 Hz. The experimental results have been verified with the theoretical expectations showing the validity of the system. This architecture may fill a performance gap in the previously proposed fiber optical shape sensors, reaching cm resolutions over hundreds of meters while maintaining the dynamic monitoring of the curvature. This proof of concept demonstrates the feasibility of the proposed technique, leading to the possibility of easily increasing the resolution by using higher RF bandwidth electronics. This work constitutes a first step in building a complete dynamic shape sensor with these features and advantages. Further improvements include the monitoring of the central core, leading to more information about shape, the implementation of field-programmable gate arrays (FPGAs) as a substitute of the AWGs (greatly reducing the cost), or the combination of this technique with quasi-integer ratio OFCs that could overcome the trade-off between range and sampling rate.

Q1 **Funding.** Ministerio de Ciencia MCIN/AEI/10.13039/501100011033 and FSE invierte en tu futuro (PRE-2019–087444); Ministerio de Ciencia MCIN/AEI/10.13039/501100011033 and European Union «NextGenerationEU»/PRTR (RYC2021-032167-I, RYC2021-035009-I); Ministerio de Ciencia MCIN/AEI/10.13039/501100011033 (INSTILL PID2020-120071RJ I00, PID2020-120071RJ I00); Comunidad de Madrid and FEDER Program (SINFOTON2-CM: S2018/NMT-4326); Ministerio de Ciencia MCIN/AEI/10.13039/501100011033 and the European Union NextGenerationEU/PRTR (PSI: PLEC2021-007875, TREMORS: CPP2021-008869); Ministerio de Ciencia MCIN/AEI/10.13039/501100011033, and FEDER Una manera de hacer Europa (PID2021-128000OB-C21, PID2021-128000OB-C22); HORIZON EUROPE European Innovation Council (SAFE: 101098992).

Acknowledgments. The work of M.S.-A. was supported by MCIN/AEI/10.13039/501100011033 and FSE invierte en tu futuro under Grant PRE-2019–087444. The work of M.R.F-R. and H.F.M. was supported by MCIN/AEI/10.13039/501100011033 and European Union NextGenerationEU/PRTR under grants RYC2021-032167-I and RYC2021-035009-I. The work of D.B. is supported by the I + D + i project INSTILL PID2020-120071RJ I00 funded by MCIN/AEI/10.13039/501100011033. This work was supported in part by Comunidad de Madrid and FEDER Program (grant SINFOTON2-CM: S2018/NMT-4326), in part by the Spanish MCIN/AEI/10.13039/501100011033 and the European Union NextGenerationEU/PRTR Program under Grant PSI ref. PLEC2021-007875 and TREMORS ref. CPP2021-008869, in part by the Spanish MCIN/AEI/10.13039/501100011033, and FEDER Una manera de hacer Europa (grants PID2021-128000OB-C21 and PID2021-128000OB-C22), and in part by the HORIZON EUROPE European Innovation Council under Grant SAFE: ref. 101098992.

Disclosures. The authors declare no conflicts of interest.

Data availability. Data underlying the results presented in this paper are not publicly available at this time but may be obtained from the authors upon reasonable request.

REFERENCES

1. F. Khan, A. Denasi, D. Barrera, J. Madrigal, S. Sales, and S. Misra, IEEE Sens. J. **19**, 5878 (2019).
2. F. Khan, D. Barrera, S. Sales, and S. Misra, Sens. Actuators, A **317**, 112442 (2021).
3. R. Ahmad, W. Ko, K. S. Feder, and P. S. Westbrook, Opt. Lett. **45**, 5189 (2020).
4. A. Motil, A. Bergman, and M. Tur, Opt. Laser Technol. **78**, 81 (2016).
5. Z. Zhao, M. A. Soto, M. Tang, and L. Thévenaz, **24**, SeM4D.4 (2016).
6. F. Monet, S. Sefati, P. Lorre, A. Poiffaut, S. Kadoury, M. Armand, I. Iordachita, and R. Kashyap, *Proc. - IEEE Int. Conf. Robot. Autom.* (2020), pp. 8877–8883.
7. Ł. Szostkiewicz, M. A. Soto, Z. Yang, A. Dominguez-Lopez, I. Parola, K. Markiewicz, A. Pytel, A. Kołakowska, M. Napierała, T. Nasiłowski, and L. Thevenaz, Opt. Express **27**, 20763 (2019).
8. M. Soriano-Amat, D. Fragas-Sánchez, H. F. Martins, D. Vallespín-Fontcuberta, J. Preciado-Garbayo, S. Martin-Lopez, M. Gonzalez-Herraez, and M. R. Fernández-Ruiz, Sensors **21**, 3766 (2021).
9. G. Tu, M. Zhao, Z. Tang, K. Qian, and B. Yu, J. Lightwave Technol. **38**, 6691 (2020).
10. Y. Koyamada, M. Imahama, K. Kubota, and K. Hogari, J. Lightwave Technol. **27**, 1142 (2009).